ORIGINAL RESEARCH

Core–Shell Imidazoline–Functionalized Mesoporous Silica Superparamagnetic Hybrid Nanoparticles as a Potential Theranostic Agent for Controlled Delivery of Platinum(II) Compound

Mehdi Abedi [1]
Samira Sadat Abolmaali [1,2]
Mozhgan Abedanzadeh [1]
Fatemeh Farjadian [2]
Soliman
Mohammadi Samani [2,3]
Ali Mohammad Tamaddon [1,2]

[1]Department of Pharmaceutical Nanotechnology, School of Pharmacy, Shiraz University of Medical Sciences, Shiraz, Fars, Iran; [2]Center for Nanotechnology in Drug Delivery, School of Pharmacy, Shiraz University of Medical Sciences, Shiraz, Fars, Iran; [3]Department of Pharmaceutics, School of Pharmacy, Shiraz University of Medical Sciences, Shiraz, Fars, Iran

Introduction: As widely used chemotherapeutic agents, platinum compounds have several therapeutic challenges, such as drug resistance and adverse effects. Theranostic systems, macromolecular or colloidal therapeutics with companion diagnostics, not only address controlled drug delivery but also enable real-time monitoring of tumor sites.

Methods: Synthesis of magnetic mesoporous silica nanoparticles (MMSNs) was performed for dual magnetic resonance imaging and drug delivery. MMSN surfaces were modified by imidazoline groups (MMSN-Imi) for cisplatin (Cis-Pt) conjugation via free N-termini to achieve well-controlled drug-release kinetics. Cis-Pt adsorption isotherms and drug-release profile at pH 5 and 7.4 were investigated using inductively coupled plasma atomic emission spectroscopy.

Results: MMSN-Imi showed a specific surface area of 517.6 m^2 g^{-1}, mean pore diameter of 3.26 nm, and saturated magnetization of 53.63 emu/g. A relatively high r_2/r_1 relaxivity value was obtained for MMSN-Imi. The nanoparticles provided high Cis-Pt loading with acceptable loading capacity (~30% w:w). Sustained release of Cis-Pt under acidic conditions led to specific inhibitory effects on the growth of human epithelial ovarian carcinoma cells, determined using MTT assays. Dual acridine orange–propidium iodide staining was investigated, confirming induction of apoptosis and necrotic cell death.

Conclusion: MMSN-Imi exhibited potential for applications in cancer chemotherapy and combined imaging.

Keywords: magnetic properties, cisplatin, SiO_2, theranostic, MRI, drug delivery

Introduction

Chemotherapy is considered a conventional therapeutic intervention in cancer patients. Cisplatin (Cis-Pt) is one of the most popular chemotherapeutic agents, interfering with DNA and cellular proliferation.[1,2] Cis-Pt is indicated in different cancers, such as lung, breast, ovary, head and neck, and testicles.[3] Despite their effectiveness, platinum(II) compounds have several therapeutic challenges, such as drug resistance and adverse drug effects.[4] Therefore, several studies have focused on the potential use of nanotechnology for the delivery of anticancer agents to improve their therapeutic effect and reduce related side effects. An ideal drug carrier should have several properties, such as high loading capacity, biocompatibility, and a controlled drug-release profile at the biological target site. Many carriers, such as hydrogels[5] and polymeric,[6] lipidic,[7] peptide,[8] and carbon based materials,[9] have been

Correspondence: Ali Mohammad Tamaddon
Department of Pharmaceutical Nanotechnology, School of Pharmacy, Shiraz University of Medical Sciences, Shiraz, Fars, Iran
Tel +98 71 32424126
Email amtamadon@gmail.com

introduced. Also, different types of inorganic nanoparticles have been used for Cis-Pt delivery, including gold nanoparticles,[10] metal–organic frameworks,[11] and porous and nonporous silica nanoparticles.[12]

Due to their unique properties, such as magnetic susceptibility, biocompatibility and ability to modify surface functionalization,[13] iron oxide magnetite nanoparticles are of great interest for various biomedical applications, including usage in magnetic hyperthermia,[14] magnetic resonance imaging (MRI),[15] photoacoustic imaging,[16] photodynamic therapy,[17,18] photo-thermal therapy,[19] biological detection,[20] magnetic bio-separation,[21] etc. Magnetic iron oxide nanoparticles can reduce transverse relaxation time, known as T_2, by producing an inhomogeneous magnetic field around the outer shell, which results in negative MR images. As such, area around the magnetic nanoparticles becomes darker.[22] For magnetite nanoparticles to be used in biomedical applications, several properties, such as small dimensions, homogeneity, superparamagnetism, and chemical and colloidal stability, are generally required. For surface functionalization, they are usually coated with certain biocompatible materials, such as polymers, silica, carbon, and surfactants, or small molecules, such as citric acid (CA), and fatty acids.[23–25] The nature of coating material is the key factor in certain cases where it can form hydrogen bonds. In such situations, surface modification can reduce particle aggregation and increase magnetite nanoparticle stability. The coating can also reduce leaching of core materials,[26] which play a significant role in retarding clearance by the reticuloendothelial system in vivo. Among the shell materials, silica acts as an inert layer, which improves the physical stability of nanoparticles in aqueous medium. Furthermore, mesoporous silica nanoparticles (MSNs) are a highly promising material, due to large surface area, biocompatibility, tunable pore size, and surface-functional groups for bioconjugation with anticancer drugs and targeting ligands. With a variety of functional groups such as carboxylic acid and amines, MSNs have been proposed as Cis-Pt carriers. Carboxylic acid–functionalized MSNs exhibit pH- and salt-induced Cis-Pt release.[25,27] Amino-functionalized MSNs show higher loading capacity than those functionalized with carboxylic acid, but retained and do not release a considerable amount of the loaded drug, possibly due to strong interactions between Cis-Pt and amino groups.[28] On the other hand, platinum can coordinate with the imidazole group, as reported for a series of cytotoxic platinum dichlorocomplexes[29,30] and imidazolefunctionalized SBA15 for solid-phase microextraction.[31] Therefore, we aimed to employ a new synthesis approach to generate imidazoline (Imi) functionality (with less basicity than aliphatic amines) on the pores of magnetic mesoporous silica hybrid nanoparticles. It was proposed that Cis-Pt molecules can be immobilized by the formation of coordination complexes, as similarly shown for various transition-metal ions that reversibly interact with nitrogen containing functional groups, such as amines and imidazole.[31–34] Interestingly, protonation of the Imi ring (imine nitrogen pKa 6.9) in an acidic tumor microenvironment can weaken Cis-Pt interaction, and consequently pH-sensitive drug release can be attained (Figure 1). In addition, magnetic mesoporous silica hybrid nanoparticles not only can load and release Cis-Pt in a controlled manner but can also act as a contrast agent for dual imaging and therapy (theranostic) application. Therefore, T_1- and T_2-weighted MR images were investigated to assess the applicability of these particles as contrast agents. Finally, cell-proliferation and dual-staining experiments were used to exhibit the feasibility of using these hybrid nanoparticles as therapeutic agents in ovarian cancer cells.

Methods
Materials
Ferric chloride hexahydrate (98%), ferrous chloride tetrahydrate, and triethoxy-3-(2-imidazoline-1-yl)propylsilane (TIP; 97%) were purchased from Sigma-Aldrich (USA). Ammonia solution (25%), ethanol (98%), CA (Ph Eur), tetraethyl orthosilicate (TEOS, 98%), cisplatin (Cis-Pt), dimethylformamide, toluene, tetrahydrofuran, acetic acid, sodium acetate, sodium chloride, potassium dihydrogen phosphate, and dipotassium hydrogen phosphate were supplied by Merck (Germany). Hexadecyltrimethylammonium bromide (CTAB) was purchased from Daejung Chemicals (South Korea). All chemicals were of reagent grade and used as received.

Synthesis of Fe_3O_4 Nanoparticles
Fe_3O_4 nanoparticles were prepared based on methodologies described in our earlier work, but with minor modification.[35] In brief, 50 mL $FeCl_2$.4 H_2O (1.35 g) and $FeCl_3$.6H_2O (3.68 g) was prepared with deionized water, then transferred to a three-necked flask and temperature gradually increased to 80°C in reflux condition under a nitrogen atmosphere. To prevent the development of large polycrystalline particles, the reaction mixture was vigorously stirred and pH adjusted 10–11 by adding NH_4OH (25 wt%). After 2 hours, the product was capped by adding 4 mL 0.5 g/mL CA solution,
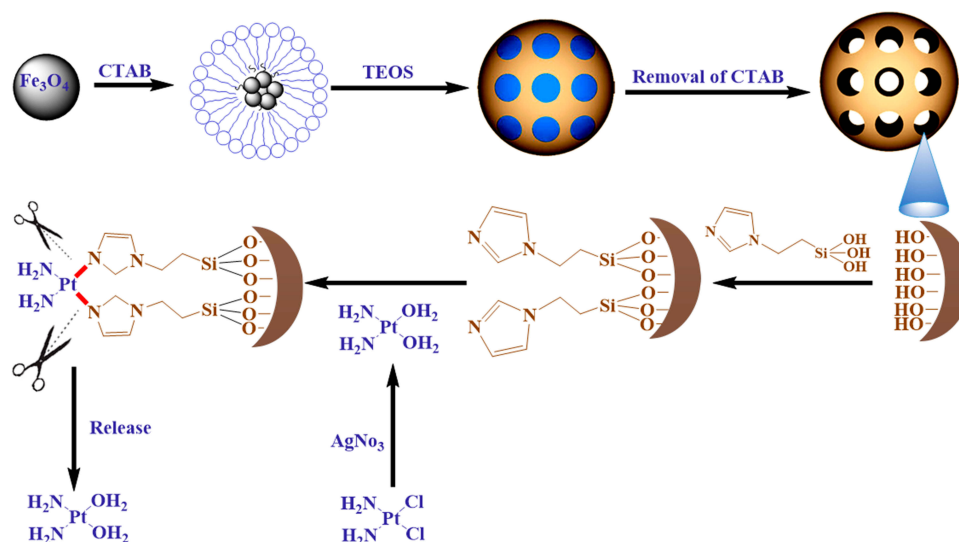
Figure 1 Schematic representation of the preparation of magnetic mesoporous silica nanoparticles functionalized with TIP (MMSN-Imi) for subsequent loading and release of aquated cisplatin.

the reaction temperature raised to 90°C, and the reaction continued for 1 hour while stirring.[35] Black precipitates were obtained by cooling the reaction mixture to room temperature, which was then thoroughly rinsed with deionized water. During each rinsing step, samples were separated by magnetic decantation. Fe_3O_4 stabilized with CA is abbreviated as Fe_3O_4-CA.

Synthesis of Imidazole-Functionalized Magnetic Mesoporous Silica

Synthesis of magnetic MSNs (MMSNs) with uniform particle-size distribution was accomplished using the sol–gel technique. Typically, 2×10^{-4} mol Fe_3O_4-CA nanoparticles were dispersed in 200 mL deionized water under bath ultrasonication for 30 minutes. Subsequently, 0.4 g CTAB was added to each Fe_3O_4-CA dispersion with vigorous stirring for 1 hour. Then, 0.234 mL TEOS was dissolved in 60 mL ethanol and added to the reaction medium dropwise in two steps with a 5-hour interval. Then, the resulting suspension was magnetically separated and washed with 20% ethanol three times to separate unreacted TEOS and ammonia.[36] Finally, the pore-generating agent (CTAB) was removed by an ethanolic solution of ammonium nitrate (NH_4NO_3, 6 g/L, 60 mL) under reflux at 60°C for 2 hours. Following magnetic separation and washing, the product was dried in an oven at 110°C for 72 hours. The experimental reaction yield of 68%±4% was obtained for three separate batches of MMSNs. Then, 100 mg of the product sample was

refluxed in 20 mL anhydrous toluene with TIP for 20 hours for surface functionalization with the Imi groups.[31] MMSN-Imi were collected and washed with anhydrous toluene three times and then dried in an oven at 110°C to remove the solvent.[37]

Loading of Cisplatin

To increase the reactive concentration of Cis-Pt in aqueous solution, chloro-ligands of the Cis-Pt were replaced by aqua-ligands. Briefly, Cis-Pt was suspended in water and mixed with $AgNO_3$ ([$AgNO_3$]/[Cis-Pt]=2). The solution was kept in the dark at 37°C for 24 hours. Then, AgCl precipitates were removed by centrifugation for 20 minutes at 12,000 rpm. The supernatant containing highly water-soluble Cis-Pt derivative was then diluted to 0.1 mg/mL by adding double-distilled water. Cis-Pt loading was achieved by direct addition of the MMSN-Imi samples (2 mg) to 1 mL Cis-Pt solution while shaking at 37°C in the dark for 24 hours. Unloaded aqua-ligands were separated by centrifuging at 12,000 rpm for 20 minutes. Supernatant analysis was carried out by inductively coupled plasma atomic emission spectroscopy for platinum concentration. The adsorption capacity of drug (q), drug loading (DL%), and loading efficiency (LE%) were calculated:[38]

$$q = (C_0 - C_e) \times V/m \qquad (1)$$

$$DL (\%) = (W_0 - W_u) \\ \times 100/(W_{MMSN-IMI} + W_0 - W_u) \qquad (2)$$

$$LE\ (\%) = (W_0 - W_u) \times 100/(W_0) \qquad (3)$$

where C_0, C_e, V, and m stand for the concentration of Cis-Pt added to the medium, equilibrium concentration of Cis-Pt, and medium volume and amount of the adsorbent MMSN-Imi, respectively. W_0 and W_u denote the respective amounts of Cis-Pt added and the unloaded drug calculated from free Cis-Pt concentration at equilibrium.

Cis-Pt–adsorption isotherms were calculated for MMSN-Imi at different drug:particle mass ratios 0.025–1. To investigate the Cis-Pt–adsorption mechanism on MMSN-Imi, data were fitted to different mathematical models: Dubinin–Raduskevich, Langmuir, Freundlich, and Temkin. The Langmuir isotherm (Equation 4) assumes monolayer adsorption on a surface containing a finite number of uniform sites. Each independent adsorbate exhibits fixed and equal adsorption energy, and any steric hindrance or side-by-side connection between the adsorbed molecules is not allowed:[39]

$$q = q_m K_l C_e/(1 + K_1 C_e) \qquad (4)$$

where q (mg/g) and q_m (mg/g) are the mass of adsorbed Cis-Pt per unit weight of MSN-Imi and maximum uptake per unit mass of MSN-Imi, respectively. C_e (mg/L) is the free equilibrium concentration of adsorbate in the solution and K_l (L/g) the Langmuir constant, which is related to the adsorption energy. The Freundlich isotherm (Equation 5) is used to describe multilayer adsorption into heterogeneous surfaces. It assumes exponential distribution of adsorption sites and energy:[40]

$$Q = K_f C_e^{1/n} \qquad (5)$$

where K_f and n (dimensionless) are the Freundlich constant and experimental parameters related to adsorption intensity. The Temkin isotherm (Equation 6) assumes heterogeneous adsorption such that energy of the adsorption layer decreases as adsorption by layer increases in a linear relationship (very low or high concentrations are neglected):

$$Qe = RT/b\ (Ln\ K_T + LnCe) \qquad (6)$$

where b is the Temkin constant, which is related to sorption heat (Jmol^{-1}), and K_T the Temkin isotherm constant (L□g^{-1}). The Dubinin–Radushkevich isotherm (Equation 7) is a semiempirical equation in which adsorption follows a pore-filling mechanism.[41] It assumes Gaussian energy distribution onto heterogeneous surfaces:

$$LnQ_e = LnQ_s - K_D\varepsilon^2 \qquad (7)$$

where Q_s is theoretical isotherm saturation capacity (mg/g), K_D the Dubinin–Radushkevich isotherm constant (mol^2/J^2),

and ε the Dubinin–Radushkevich isotherm constant. Isotherm parameters were computed by linear transformation of the experimental results. The correlation coefficient (R^2) was also used to determine the best-fitting adsorption isotherm to the experimental data.

Kinetics of Cis-Pt Release

To evaluate in vitro drug-release kinetics, 2 mg Cis-Pt–loaded MMSN-Imi samples were dispersed separately by bath sonication for 10 seconds in PBS (pH 7.4) or acetate buffer saline (pH 5), dispensed in 2 mL microtubes, and were placed in a tube-revolver rotating mixer at 37°C in the dark. Samples were withdrawn at fixed time intervals, followed by measurement concentration of Cis-Pt with inductively coupled plasma atomic emission spectroscopy. Drug-release data were fitted with different mathematical models — including zero-order, first-order, Higuchi, and Korsmeyer–Peppas — for further investigation of the drug-release mechanism.

Hemolysis Assays

Hemolysis assays were performed to investigate the effect of surface chemistry and protein corona of the hybrid nanoparticles on lysis of human red blood cells.[42] Briefly, 5 mL whole human blood was obtained according to the standard operating procedure approved by the Institutional Review Board of the Iran Blood Transfusion Organization for venous blood collection, treatment, and disposal from a healthy volunteer who had read and signed written informed consent. Then, the blood was transferred to a sterile microtube containing 200 μL 50 mg/mL EDTA, centrifuged at 800 g for 10 minutes at 4°C, the serum layer removed, and the remaining red blood cells pooled and washed five times with isotonic PBS. MMSN-Imi were dispersed in PBS by ultrasonication at various concentrations — from 50–1,000 μg/mL. Subsequently, 22 μL 10× diluted red blood cells were incubated with 200 mL dispersed particles. After 2 hours' shaking (Orbital shaker, 100 rpm) at 37°C, the mixtures were centrifuged at 200 g for 10 minutes and UV-vis absorbance of the supernatants determined at λ=540 nm. To investigate the possible role of serum-protein adsorption on hemocompatibility, the particles were incubated in isolated human blood serum for 30 minutes at 37°C, then were centrifuged and washed three times with PBS. Protein corona–coated MSNs (MMSN-Imi-PC) were dispersed in PBS and using ultrasound probe at power of 10% for 2 minutes, and the hemolysis assay was repeated according to the described method. The percentage of hemolysis was determined:

$$Hemolysis \; (\%) \; = \; (A - A_0)/(A_{max} - A_0) \times 100 \quad (8)$$

where A, A_0 and A_{max} are the respective absorbance of samples and negative (isotonic PBS (pH= 7.4) and positive (double-distilled water) controls.

In Vitro Cytotoxicity

Cytotoxicity of free Cis-Pt, MMSN-Imi, and MMSN-Imi-Cis-Pt was evaluated against A2780 human epithelial ovarian carcinoma cells (obtained from the Pasteur Institute of Iran) using MTT assays. Cells were cultured in 96-well microplates at a density of 10^{-4} cells per well in RPMI 1640 supplemented with 10% (v:v) FBS at 37°C in a humidified incubator with 5% CO_2. After incubation for 24 hours, the culture medium was discarded and the cells treated with 100 μL of each sample prepared in complete culture medium by serial dilution. Cis-Pt concentration was set to 1–100 μg/mL. After 48 hours, the culture medium was aspirated, the MTT reagent (0.5 mg/mL) immediately added, and the plates incubated for 4 hours. Upon removal of the MTT solution, the purple formazan crystals were dissolved in 100 μL DMSO, and absorbance was read at 570 nm with reference wavelength of 650 nm using a microplate reader (BioTek, USA).

Dual AO–PI Fluorescence Staining

Dual acridine orange (AO)–propidium iodide (PI) cell staining was used to visualize nuclear changes and apoptotic body formation following treatment of cells with each sample. For this purpose, A2780 cells were cultured with RPMI 1640 complete medium on coverslips in six-well plate (2×10^5 cells per well) for 48 hours. Then, the medium was removed and cells treated with MMSN-Imi, MMSN-Imi–Cis-Pt, and free Cis-Pt for a further 48 hours, media removed, and cells were incubated with 1 mL AO–PI staining solution for 30 minutes. Stained cells were visualized under fluorescent microscopy to assess apoptotic and necrotic morphological changes.[43]

MRI Studies and Relaxometric Properties

To determine T_1- and T_2-weighted MRI contrast effects of MMSN-Imi, different concentrations of MMSN-Imi (containing 0.1, 0.2, 0.3, 0.4, 0.5, and 0.6 mM Fe) were dispersed in deionized water at 20°C by ultrasonication and relaxation times were analyzed by 1.5 T MRI (Magnetom Avanto, Siemens), as reported elsewhere.[44] Briefly, T_2-weighted images were captured at a predefined spin-echo sequence with repetition time of 1,600 ms and echo times of 10, 43,

75, and 107 ms under field of view 238, turbo factor 18, and slice thickness 7.5 mm. Similarly, T_1-weighted images were acquired at the predefined repetitions of 100, 1550, 3,150 and 4,750 ms and echo time of 18 ms.

Results and Discussion
FT-IR Spectra Analysis

To confirm the presence of silica and Imi on the surfaces of coated magnetic nanoparticles, Fe_3O_4-CA, MMSN, and MMSN-Imi were characterized by FT-IR spectroscopy. As shown in Figure 2A, all samples showed wide peaks at around 3,400 cm^{-1}, which was related to O–H stretching. The IR spectrum of the Fe_3O_4-CA sample showed two signals that appeared at 578 cm^{-1} and 1,396 cm^{-1}, attributed to Fe–O bonds and C–O stretching of CA carboxylate groups. Wide bands of Si–O–Si vibration appeared at 1,074 - cm^{-1} for silica-coated particles (MMSN and MMSN-Imi). Also, MMSN and MMSN-Imi showed two small adsorption peaks at 2,881 cm^{-1} and 2,935 cm^{-1} that corresponded to C–H stretching of the alkyl chain. For MMSN-Imi, two characteristic signals appeared at 1,658 cm^{-1} and 1,442 cm^{-1}, which corresponded to C=N and C–C stretching in the Imi ring.

X-Ray Diffraction Analysis

The crystalline structure of the magnetic nanoparticles was investigated before (Fe_3O_4-CA) and after silica (MMSN-Imi) coating, using X-ray diffraction (XRD). As shown in Figure 2B, Fe_3O_4-CA exhibited a series of characteristic peaks at (111), (220), (311), (222), (400), (422), (511), and (440), which belonged to the spinel phase of Fe_3O_4 (Joint Committee on Powder Diffraction Standards 894319, 19–0629).[45] Appearance of all corresponding peaks of Fe_3O_4 in the XRD spectrum of MMSN-Imi indicated that the crystalline cubic spinel of the Fe_3O_4 structure was preserved without any change in the crystalline structure during silica coating. However, a new wide peak in the XRD spectra of MMSN-Imi was noticed at 2θ=7°–20°, which belongs to the amorphous silica shell created on the surface of Fe_3O_4-CA nanoparticles, as reported in the literature.[46]

N_2 Adsorption–Desorption Isotherm

Figure 2C depicts an type IV adsorption–desorption isotherm following the International Union of Pure and Applied Chemistry classification, revealing the mesoporous nature of the coated silica. The adsorption isotherm clearly
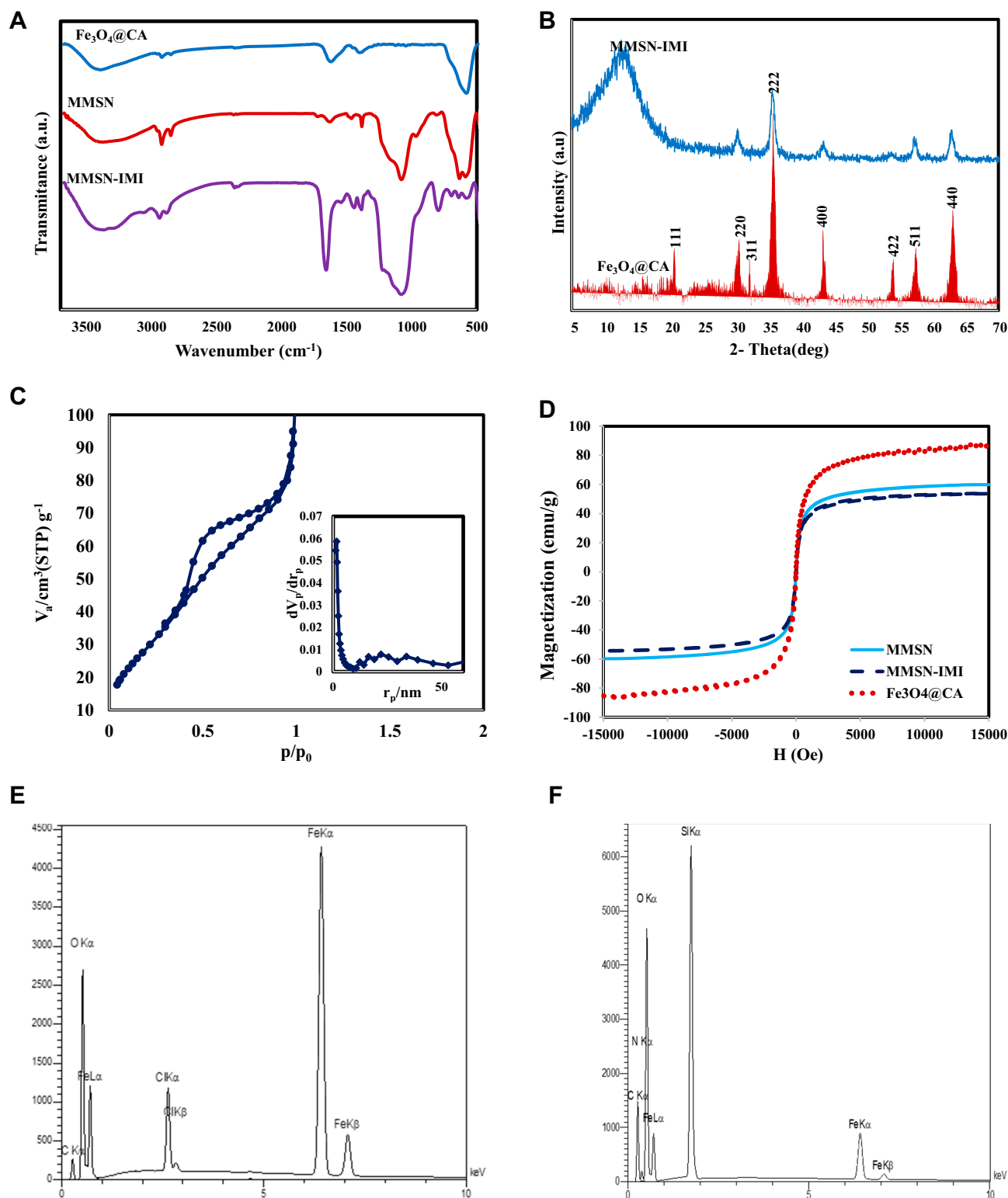
Figure 2 (**A**) FTIR spectra of Fe₃O₄-CA, MMSN, and MMSN-Imi; (**B**) XRD patterns of as-prepared Fe₃O₄-CA, MMSN and MMSN-Imi; (**C**) nitrogen adsorption–desorption isotherm (inset BJH pore-size distribution of MMSN-Imi); (**D**) magnetic hysteresis curves of magnetic nanoparticles; EDX spectra of Fe₃O₄-CA (**E**) and MMSN-Imi (**F**).

showed monolayer gas adsorption on the pore surface at low partial pressure, followed by multilayer gas adsorption at high partial pressure. There was no limiting adsorption of N_2 gas at high partial pressure, suggesting the presence of macrospores.[44] This finding was in line with the wide distribution of pore size diameter (the maximum frequency

was calculated at 3.26 nm). As an indication of capillary condensation in the mesoporous material, the hysteresis loop was shown on the desorption isotherm down to a partial pressure of around 0.25. The hysteresis loop belongs to the type H3 hysteresis loop, which is a characteristic of funnel-shaped pores.

Vibration Sample Magnetometry

Magnetization curves of Fe_3O_4-CA, MMSN, and MMSN-Imi are compared in Figure 2D. All samples presented superparamagnetic features. The saturation magnetization value of Fe_3O_4-CA was 86 emu/g, which was higher than those of MMSN and MMSN-Imi (59 and 53 emu/g, respectively). This can be due to the formation of a magnetic dead layer on the surface of Fe_3O_4-CA after silica coating. A slight decrease in saturation magnetization of MMSN-Imi (approximately 6 emu/g) can be due to immobilization of TIP on the MMSN surface and diamagnetic nature of the silica shell.[47]

Energy-Dispersive X-Ray Analysis

Energy-dispersive X-ray (EDX) spectra of the Fe_3O_4-CA and MMSN-Imi revealed the elemental composition of each sample. Unlike Fe_3O_4-CA, which only presents the existence of C, O, and Fe atoms (Figure 2E), the EDX spectrum of MMSN-Imi (Figure 2F) consists of C, N, O, Si, and Fe atoms. As expected, the presence of Si and N atoms confirmed the coating of Fe_3O_4-CA with silica and immobilization of Imi on the surface of MMSN. Table 1 presents the percentage of Fe, Si, N, C, and O in Fe_3O_4-CA and MMSN-Imi.

Scanning Electron–Microscopy Analysis

Size and surface morphology of the nanoparticles produced were characterized by transmission electron microscopy (TEM) and field emission scanning electron (FESEM) microscopy. The FESEM image in Figure 3A shows that MMSN-Imi were spherical with overall size of 50–140 nm. Also, uniform discrete particles of average size 98 nm and magnetic cores are shown in the TEM image of MMSN-Imi (Figure 3B).

Table 1 Elemental EDX data for Fe_3O_4-CA and MMSN-Imi

	Fe (%)	Si (%)	C (%)	O (%)	N (%)
Fe_3O_4-CA	52.6±2.7	—	12.1±2.2	30.8±2.7	—
MMSN-Imi	6.4±1.1	8.7±1.0	27.2±2.2	51.2±2.1	7.4±0.2

Dynamic Light Scattering

Hydrodynamic diameters of the nanoparticles were determined by dynamic light scattering. Figure 4, A–D shows both frequency distribution and cumulative particle-size distribution of Fe_3O_4-CA, MMSN and MMSN-Imi, respectively. Mean size (intensity diameter) and polydispersity index (PDI) values varied among the samples: Fe_3O_4-CA 10±1.2 nm, PDI 0.22, MMSN 100±11 nm, PDI 0.25, MMSN-Imi 121±10 nm, PDI 0.25, human serum–protein adsorbed MMSN-Imi (321 ±18 nm, PDI 0.23). The histograms show a unimodal Gaussian distribution for all samples. As was expected for multinuclear core–shell nanoparticles, the mean particle size of Fe_3O_4-CA nanoparticles increased considerably for silica-coated ones. Due to human serum–protein coating of the nanoparticles (MMSN-Imi-PC), particle size increased further, as previously reported.[48]

Due to interactions and adsorption of some components in the cell-culture medium, such as proteins on the surfaces of nanoparticles, particle size, surface charge, and functionality of the nanoparticles can be altered.[49] Colloidal stability of MMSN-Imi was determined in RPMI 1640 medium containing 25 mM HEPES buffer, NaCl (5.5 g/L), and sodium bicarbonate buffer (2 g/L) by dynamic light scattering. It was shown that MMSN-Imi sizes increased to 225±23 nm. It seems that addition of salts available in the cell-culture medium can influence the electrical double layer and the colloidal stability of MMSN-Imi, leading to modest particle aggregation. Moreover, surface adsorption of amino acids and proteins can be responsible for increased particle size.

ζ-Potential Measurement

ζ-potential measurements were made to infer possible changes in surface electric potential of the magnetic nanoparticles after silica coating and stability of the nanoparticles.[50] Higher ζ-potential values, either negative or positive, are necessary to ensure stability and to avoid aggregation of particles. Fe_3O_4-CA, MMSN, and MMSN-Imi showed average ζ-potential of −73.6±9.8, −53.9±4.4, and −46.1±4.2 mV. Considering that ζ-potential >30 mV or <−30 mV indicates colloidal stability,[51] it is suggested that MMSN-Imi can exhibit adequate stability in physiological conditions, due to high electrostatic repulsion between particles, but further investigation is warranted.[51] Negative ζ-potentials are attributed to the surface-immobilized CAs (Fe_3O_4-CA) and ionized surface silica (MMSN and MMSN-Imi). The ζ-potential of protein-coated MMSN-Imi (MMSN-Imi-PC) was reduced to −37.4±5.9 mV,
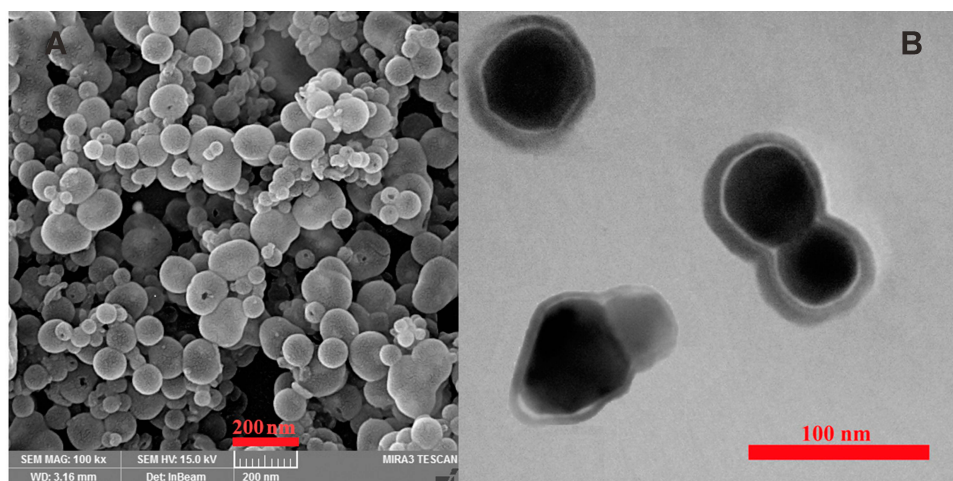
Figure 3 (**A**) FESEM and (**B**) TEM of MMSN-Imi.

which was expected due to adsorption of serum proteins, such as albumin, the most abundant protein in human blood serum.[52]

Cis-Pt Loading

MMSN-Imi samples were loaded with Cis-Pt using direct incubation with Cis solution at various concentrations, in order to obtain Cis-Pt–loaded particles (MMSN-Imi-Cis-Pt). DL% and LE% are shown in Figure 5A. The highest LE of 58% at drug:particle ratio of 0.5 and DL of 30% were achieved at the higher drug:particle ratio of 1, quite superior to those of other carriers reported elsewhere in the literature.[53–57]

The high DL% can be attributed to the pore geometry (H_3 hysteresis, funnel-shaped) and drug–matrix interactions through different mechanisms, such as coordination between platinum ions and the Imi group or H-bonds between Cis-Pt amines and silica hydroxyls. It was also observed that by increasing the drug:particle ratio, both LE
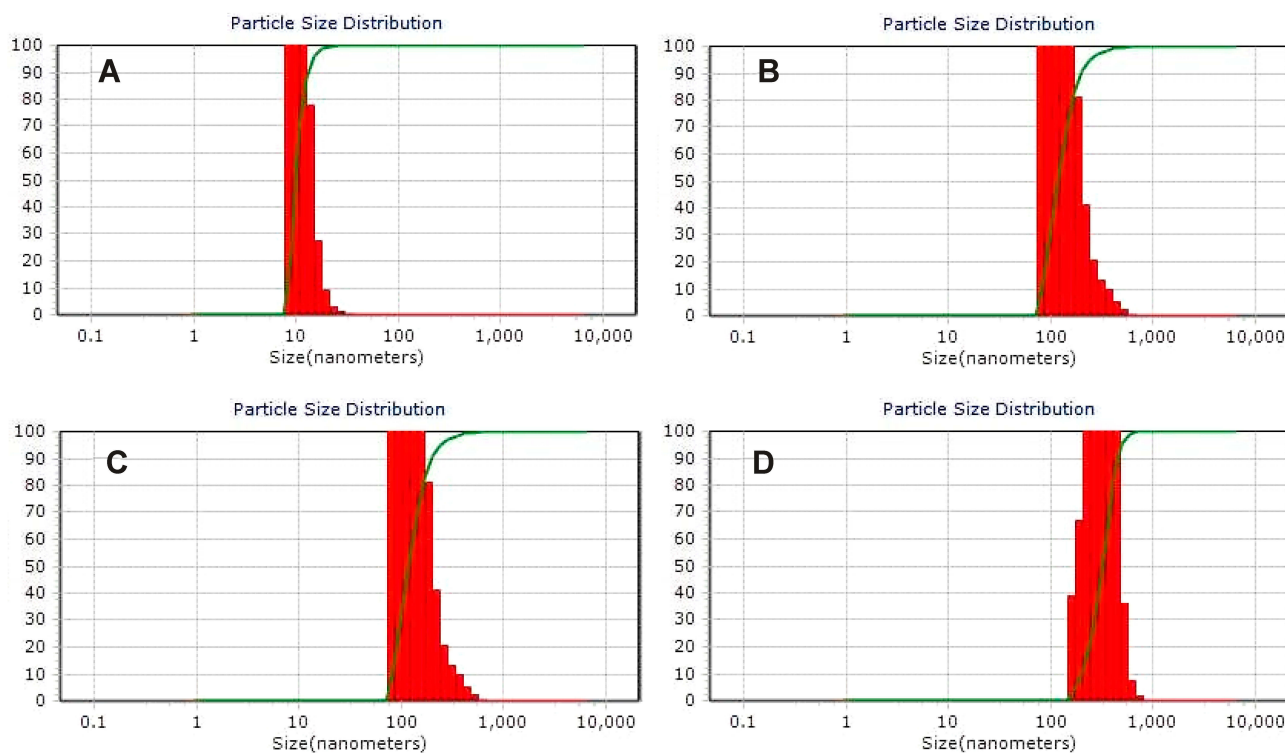

Figure 4 Particle size-distribution of (**A**) Fe_3O_4-CA, (**B**) MMSN, (**C**) MMSN-Imi, and (**D**) MMSN-Imi-PC (postincubation with human-serum proteins).
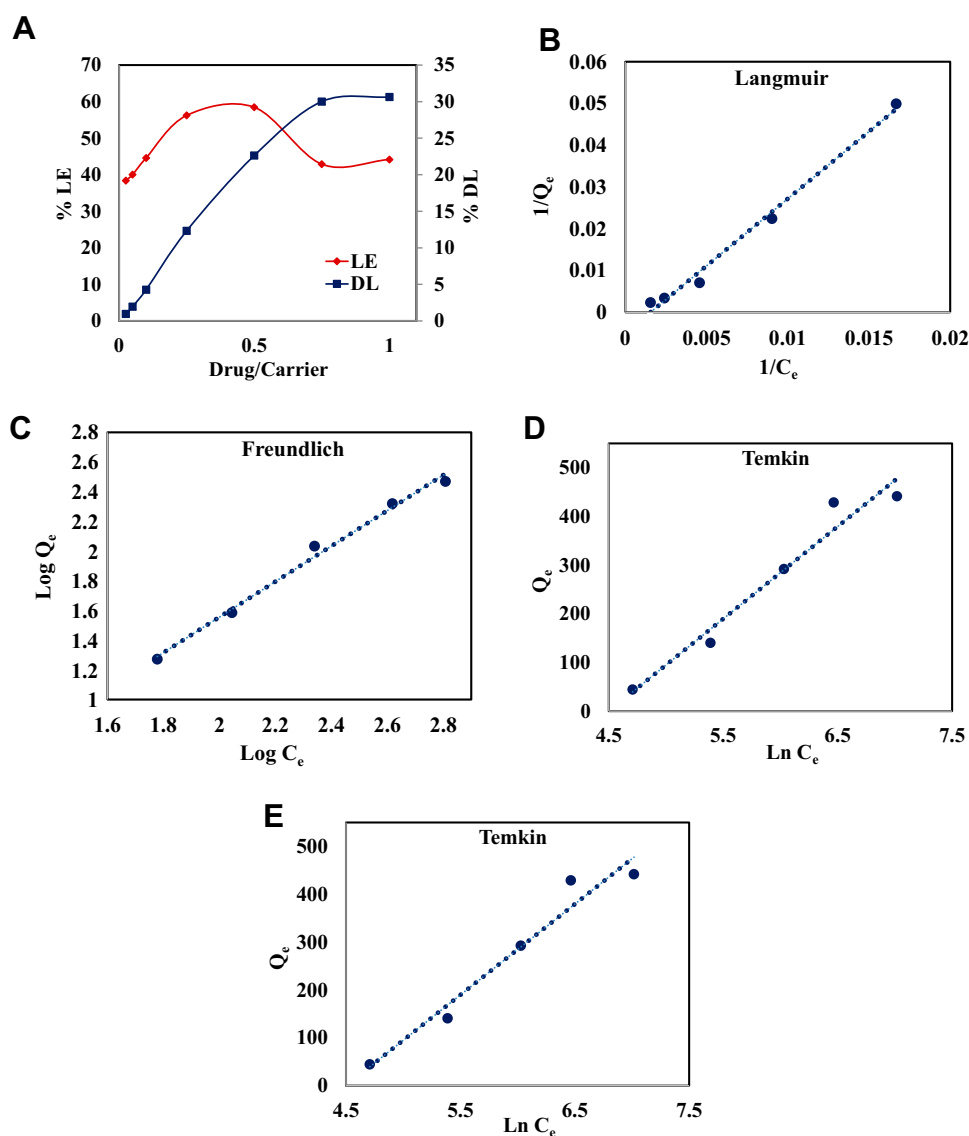
Figure 5 (**A**) Drug loading (DL%) and loading efficiency (LE%) against Cis-Pt–MMSN-Imi mass ratio. Experimental drug-loading data were fitted onto (**B**) Langmuir, (**C**) Freundlich, (**D**) Temkin, and (**E**) Dubinin–Radushkevich adsorption isotherms.

% and DL% increased; however, with drug:particle ratios >0.5, LE % was reduced. Therefore, a drug:particle mass ratio of 0.5 was chosen as optimum.

To investigate the Cis-Pt–loading mechanism, experimental data were fitted to various adsorption isotherms: Langmuir (Figure 5B), Freundlich (Figure 5C), Temkin (Figure 5D), and Dubinin–Raduskevich (Figure 5E). Table 2 presents model parameters and correlation coefficients (R^2) indicating that Freundlich adsorption was the best-fit model for Cis-Pt adsorption on MMSN-Imi (R^2=0.991). The Freundlich n parameter was <1, hence chemical processes might have been involved in drug adsorption.[58]

Release of Cis-Pt

Cis-Pt–release profiles from MMSN-Imi at pH 5 and 7.4 are summarized in Figure 6 (Figure 6A, zero-order model; Figure 6B, first-order model; Figure 6C, Higuchi model; Figure 6D, Korsmeyer–Peppas model) It was found that drug release was sustained similarly at both pH values. Moreover, no significant burst release was noticed. These particles showed a sustained release pattern during 148 hours, significantly more prolonged than previous reports.[54,56,59] There are several factors explaining "spatially hindered" diffusion of drug molecules in mesoporous materials, such as pore size, attraction to pore walls, pore opening, and the ratio of particle size to pore size.[60] It

Table 2 Adsorption isotherm parameters for Cis-Pt and MMSN-lmi

Langmuir			Freundlich			Dubinin-Radushkevich			Temkin		
Q_m (mg/g)	K_L (L/g)	R^2	K_F (L/g)	N	R^2	Q_s (mg/g)	K_D (mol^2/kJ^2)	R^2	K_T (L/g)	B (J/mol)	R^2
200	0.016	0.989	0.091	0.753	0.991	374.65	0.0045	0.93	0.011	13.06	0.977

seems that the small pores of MMSN-Imi and possible interaction between Cis-Pt and Imi–functionalized silica surface resulted in sustained drug release. Interestingly, cumulative released Cis-Pt in pH 5 was significantly >7.4, hence Cis-Pt release was responsive to acidic tumor milieu. Total Cis-Pt released after 148 hours was 77% and 60% at pH 5 and 7.4. This finding is consistent with pH sensitivity of transition-metal coordination with imidazole functional groups.[33] To investigate the underlying mechanism of drug release, data were fitted to zero-order, first-order, Higuchi, and Korsmeyer–Peppas models. As shown in Table 3, release data fitted well to the Korsmeyer–Peppas equation, which is generally recognized as a mathematical model describing drug-release mechanism. It was noticed that non-Fickian drug diffusion from the spherical porous silica matrix can be considered the main release mechanism.[61]

Hemolysis Assays

Hemolysis assays were used to assess the effect of surface functionalization with the Imi group on lysis of red blood cells before and after incubation with the serum proteins. As shown in Figure 7A, hemolytic activity increased significantly by increasing nanoparticle concentration and reached 36% in 1,000 μg/mL, significantly lower than hemolytic activity reported for MSNs in the literature.[48,62] Interestingly, it was found that serum-protein adsorption on particle surfaces attenuated the hemolytic effect exerted by MMSN-Imi. This could be explained by either surface chemistry (ie, shielding effect of serum proteins on silanol groups residing on the surface of the silica coat), ζ-potential reduction, or size effect. It has been shown that smaller particles produce more hemolytic activity than larger particles, due to the former having more surface area interacting with red blood cells to induce hemolysis.[63]
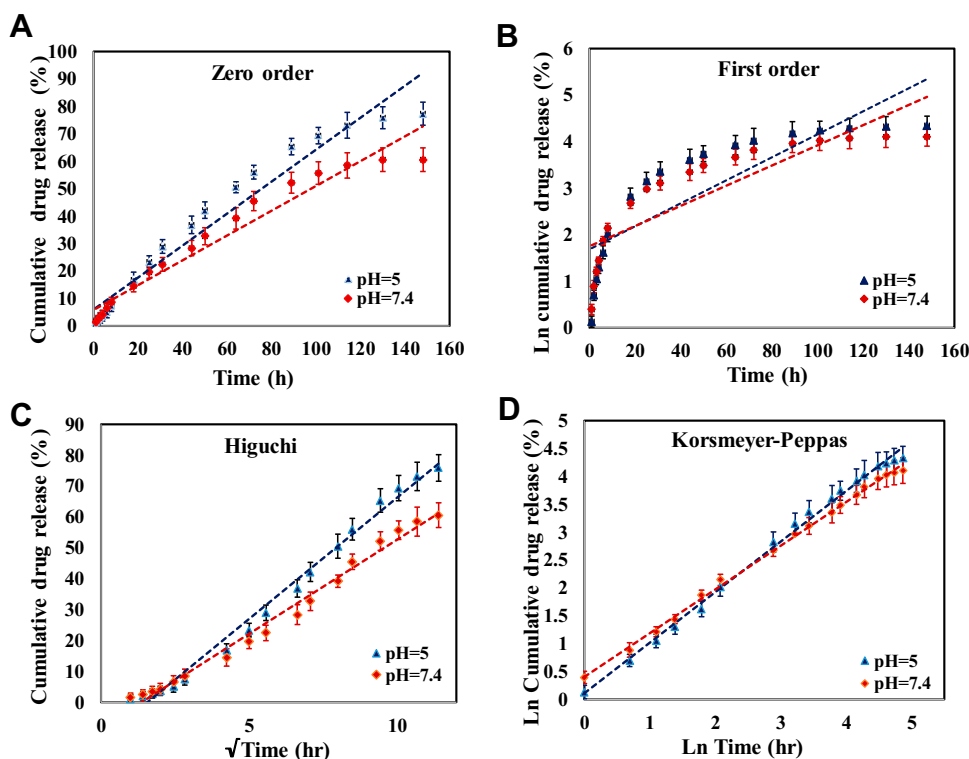

Figure 6 Drug-release profile from Cis-Pt–loaded MMSN-lmi in pH 7.4 and pH 5 according to (**A**) zero-order, (**B**) first-order, (**C**) Higuchi, and (**D**) Korsmeyer–Peppas kinetic models.

Table 3 Release-kinetic parameters and correlation coefficients (R^2) of Cis-Pt-loaded MMSN-Imi for various mathematical models

Release medium pH	Zero-order		First-order		Higuchi		Korsmeyer–Peppas	
	K^0	R^2	Q_{inf}	R^2	K_h	R^2	N	R^2
5	0.582	0.951	1.589	0.733	7.856	0.989	0.906	0.998
7.4	0.452	0.952	1.688	0.753	6.101	0.988	0.784	0.995

In Vitro Cytotoxicity

To investigate the influences particle loaded Cis-Pt on A2780-cell viability, cancer cells were exposed to free unloaded Cis-Pt and drug-loaded MMSN-Imi for 48 hours. MTT assays revealed that Cis-Pt–loaded particles had a concentration-dependent suppressive effect on the growth of cancer cells (Figure 7B) that was comparable to free Cis-Pt. IC_{50} values were calculated: 1.19 and 1.23 μM for free Cis-Pt and Cis-Pt–loaded MMSN-Imi, respectively, consistent with other reports on A2780 cells.[64–66] Interestingly, unloaded particles showed only minor cytotoxicity, even in high concentrations, confirming that drug release from MMSN-Imi resulted in significant cytotoxicity in vitro.

AO–PI Double-Staining and Fluorescence Microscopy

Following exposure to either Cis-Pt or MMSN-Imi Cis-Pt for 48 hours, A2780 cells were dual-stained by AO–PI, which confirms membrane-permeability changes typical of apoptosis.[67] Late-stage apoptotic cells with concentrated and asymmetric localization of orange fluorescence were similarly detected for Cis-Pt and Cis-Pt–loaded MMSN-Imi, whereas no significant apoptosis was detected in the negative-control group. As shown in Figure 8, more necrotic cells with increased volume and uneven fluorescence at their periphery were noticed for Cis-Pt–loaded MMSN-Imi, as similarly reported in the literature.[68]
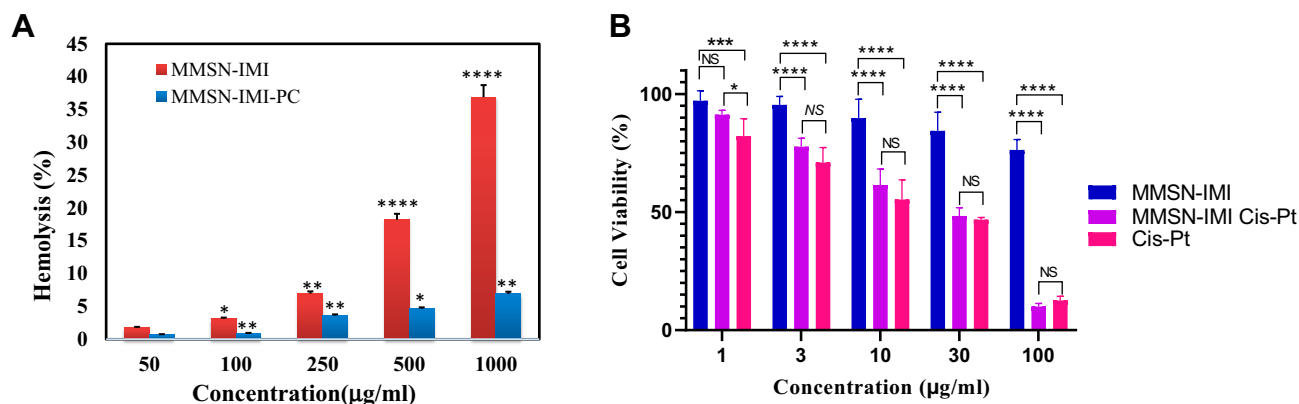

Figure 7 (**A**) Percentage of hemolysis induced by MMSN-Imi before and after incubation with human-serum proteins. (**B**) Viability of A2780 ovary cancer cells determined by MTT assay after 48 hours' exposure to different concentrations of Cis-Pt, MMSN-Imi, and MMSN-Imi–Cis-Pt. Data were generated from at least three independent experiments.
Notes: *$P \leq 0.5$; **$P \leq 0.01$; ***$P \leq 0.001$; ****$P \leq 0.0001$.
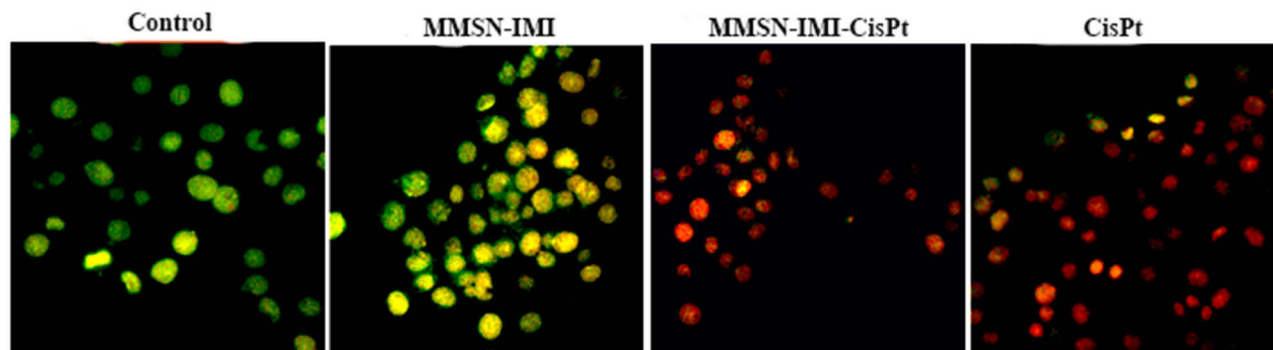**Abbreviations**: NS, not significant; PC, protein corona.

Figure 8 Fluorescent images of AO–PI dual-stained A2780 ovary cancer cells treated with either free Cis-Pt or MMSN-Imi–Cis-Pt versus untreated control cells.

T$_1$ and T$_2$ Relaxivity

Under magnetic fields, magnetic nanoparticles as MRI-contrast agents produce a magnetic dipole moment that influences water molecules around the nanoparticles.[69] Water-molecule protons in the area of magnetic field gradients created by magnetic nanoparticles can experience spin dephasing. Consequently, relaxation time is reduced by an outer-sphere mechanism that causes reduced signal intensity on T$_2$-we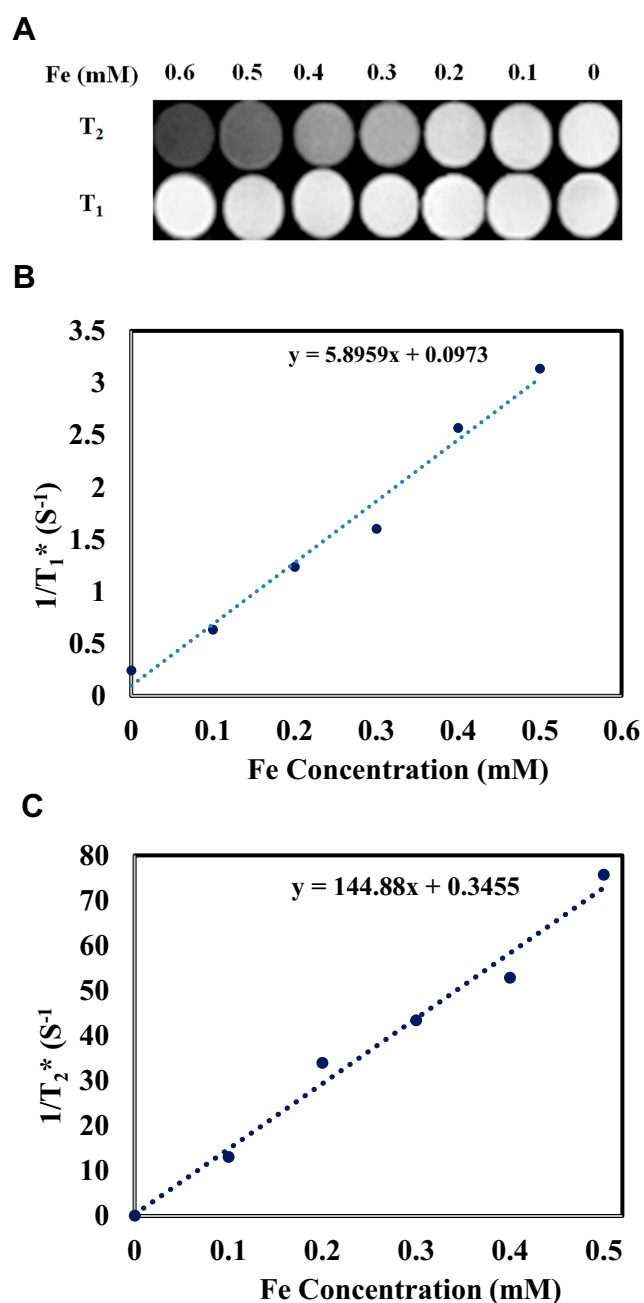ighted images.[70] As shown in Figure 9A, by increasing Fe concentrations, T$_2$-weighted images of MMSN-Imi became distinctly darker, indicating that MMSN-Imi can act as an MRI-contrast agent on T$_2$-weighted images. No substantial change was observed for T$_1$-weighted images. T$_1$ and T$_2$ relaxivity of MMSN-Imi were determined to be 5.89 and 144.88 m/M□s^{-1} (Figure 9, B and C, respectively); therefore, the r$_2$:r$_1$ ratio was calculated as 24.59, consistent with other reports on F$_3$O$_4$-coated nanoparticles.[71,72]

Conclusion

A novel theranostic platform was developed based on an Imi-functionalized magnetic mesoporous nanocarrier for Cis-Pt delivery. These particles provided unique advantages, such as high magnetism saturation (53 emu/g), high drug loading (~30% w:), and sustained and pH-triggered release of Cis-Pt without any burst, and are suitable for drug-targeting purposes. They also exhibited favorable hemocompatibility following exposure to red blood cells. Moreover, high transverse relaxivity (144.88 m/M s^{-1}) related to MMSN-Imi can be applied in MRI. In addition, the cell-viability experiments revealed that these hybrid nanoparticles (MMSN-Imi) were atoxic, yet showed specific anticancer effects if loaded with Cis-Pt (IC$_{50}$ =1.23 μM). Therefore, this carrier can be suggested for in vivo investigations.

Acknowledgments

Disclosure

The authors report no conflicts of interest in this work.

Figure 9 T$_1$ and T$_2$-weighted MR images of MMSN-Imi (**A**), linear fitting of 1/T$_1$ (**B**), and 1/T$_2$ values (**C**) at different Fe concentrations.

References

1. Kitao H, Iimori M, Kataoka Y, et al. DNA replication stress and cancer chemotherapy. *Cancer Sci*. 2018;109(2):264–271. doi:10.1111/cas.13455
2. Abedi M, Bathaie SZ, Mousavi MF. Interaction between DNA and some salicylic acid derivatives and characterization of their DNA targets. *Electroanalysis*. 2013;25(11):2547–2556. doi:10.1002/elan.201300342

3. Ma P, Xiao H, Li C, et al. Inorganic nanocarriers for platinum drug delivery. *Mater Today*. 2015;18(10):554–564. doi:10.1016/j.mattod.2015.05.017

4. Oun R, Moussa YE, Wheate NJ. The side effects of platinum-based chemotherapy drugs: a review for chemists. *Dalton Trans*. 2018;47 (19):6645–6653. doi:10.1039/C8DT00838H

5. Zheng Y, Wang W, Zhao J, et al. Preparation of injectable temperature-sensitive chitosan-based hydrogel for combined hyperthermia and chemotherapy of colon cancer. *Carbohydr Polym*. 2019;222:115039. doi:10.1016/j.carbpol.2019.115039

6. Tian J, Min Y, Rodgers Z, et al. Co-delivery of paclitaxel and cisplatin with biocompatible PLGA-PEG nanoparticles enhances chemoradiotherapy in non-small cell lung cancer models. *J Mater Chem B*. 2017;5(30):6049–6057. doi:10.1039/C7TB01370A

7. Liu B, Han L, Liu J, Han S, Chen Z, Jiang L. Co-delivery of paclitaxel and TOS-cisplatin via TAT-targeted solid lipid nanoparticles with synergistic antitumor activity against cervical cancer. *Int J Nanomed*. 2017;12:955–968. doi:10.2147/IJN.S115136

8. Lai Y, Zhao P, Zhang Z, Li B, Wu J. An effective peptide cargo carrier for the delivery of cisplatin in ovarian cancer cells. *Dyes Pigm*. 2017;143:342–347. doi:10.1016/j.dyepig.2017.04.025

9. Borandeh S, Abdolmaleki A, Abolmaali SS, Tamaddon AM. Synthesis, structural and in-vitro characterization of β-cyclodextrin grafted L-phenylalanine functionalized graphene oxide nanocomposite: a versatile nanocarrier for pH-sensitive doxorubicin delivery. *Carbohydr Polym*. 2018;201:151–161. doi:10.1016/j.carbpol.2018.08.064

10. Zhao X, Pan J, Li W, Yang W, Qin L, Pan Y. Gold nanoparticles enhance cisplatin delivery and potentiate chemotherapy by decompressing colorectal cancer vessels. *Int J Nanomed*. 2018;13:6207–6221. doi:10.2147/IJN.S176928

11. Li Y, Gao Z, Chen F, et al. Decoration of cisplatin on 2D metal–organic frameworks for enhanced anticancer effects through highly increased reactive oxygen species generation. *ACS Appl Mater Interfaces*. 2018;10(37):30930–30935. doi:10.1021/acsami.8b12800

12. Varache M, Bezverkhyy I, Weber G, et al. Loading of cisplatin into mesoporous silica nanoparticles: effect of surface functionalization. *Langmuir*. 2019;35(27):8984–8995. doi:10.1021/acs.langmuir.9b00954

13. Noqta OA, Aziz AA, Usman IA, Bououdina M. Recent advances in iron oxide nanoparticles (IONPs): synthesis and surface modification for biomedical applications. *J Supercond Nov Magn*. 2019;32 (4):779–795. doi:10.1007/s10948-018-4939-6

14. León Félix L, Sanz B, Sebastián V, et al. Gold-decorated magnetic nanoparticles design for hyperthermia applications and as a potential platform for their surface-functionalization. *Sci Rep*. 2019;9(1):4185. doi:10.1038/s41598-019-40769-2

15. Khmara I, Strbak O, Zavisova V, et al. Chitosan-stabilized iron oxide nanoparticles for magnetic resonance imaging. *J Magn Magn Mater*. 2019;474:319–325. doi:10.1016/j.jmmm.2018.11.026

16. Liu J, Guo X, Luo Z, Zhang J, Li M, Cai K. Hierarchically stimuli-responsive nanovectors for improved tumor penetration and programed tumor therapy. *Nanoscale*. 2018;10(28):13737–13750. doi:10.1039/C8NR02971G

17. Zhang J, Weng L, Su X, et al. Cisplatin and doxorubicin high-loaded nanodrug based on biocompatible thioether- and ethane-bridged hollow mesoporous organosilica nanoparticles. *J Colloid Interface Sci*. 2018;513:214–221. doi:10.1016/j.jcis.2017.10.116

18. Guo B, Zhao J, Zhang Z, An X, Huang M, Wang S. Intelligent nanoenzyme for T1-weighted MRI guided theranostic applications. *Chem Eng J*. 2019;123609. doi:10.1016/j.cej.2019.123609

19. Beik J, Asadi M, Khoei S, et al. Simulation-guided photothermal therapy using MRI-traceable iron oxide-gold nanoparticle. *J Photochem Photobio B-Biol*. 2019;199:111599. doi:10.1016/j.jphotobiol.2019.111599

20. Vallabani NVS, Singh S. Recent advances and future prospects of iron oxide nanoparticles in biomedicine and diagnostics. *3 Biotech*. 2018;8(6):279. doi:10.1007/s13205-018-1286-z

21. Fahmy SA, Alawak M, Brüßler J, et al. Nanoenabled bioseparations: current developments and future prospects. *Biomed Res Int*. 2019;2019:15. doi:10.1155/2019/4983291

22. Thapa B, Diaz-Diestra D, Beltran-Huarac J, Weiner BR, Morell G. Enhanced MRI T (2) relaxivity in contrast-probed anchor-free PEGylated iron oxide nanoparticles. *Nanoscale Res Lett*. 2017;12 (1):312.

23. Lassenberger A, Scheberl A, Stadlbauer A, Stiglbauer A, Helbich T, Reimhult E. Individually stabilized, superparamagnetic nanoparticles with controlled shell and size leading to exceptional stealth properties and high relaxivities. *ACS Appl Mater Interfaces*. 2017;9 (4):3343–3353. doi:10.1021/acsami.6b12932

24. Cîrcu M, Nan A, Borodi G, Liebscher J, Turcu R. Refinement of magnetite nanoparticles by coating with organic stabilizers. *Nanomaterials*. 2016;6(12):228. doi:10.3390/nano6120228

25. Abedi M, Abolmaali SS, Abedanzadeh M, Borandeh S, Samani SM, Tamaddon AM. Citric acid functionalized silane coupling versus post-grafting strategy for dual pH and saline responsive delivery of cisplatin by Fe3O4/carboxyl functionalized mesoporous SiO2 hybrid nanoparticles: A-synthesis, physicochemical and biological characterization. *Mater Sci Eng C*. 2019;104:109922.

26. Zhang L, Xiong Z, Zhang L, Yu B, Zhang W. Magnetic nanoparticles coated with dithizone-modified chitosan for use in solid-phase extraction of copper(ii). *Analytical Methods*. 2015;7(5):2050–2054. doi:10.1039/C4AY02596B

27. Li H, Yu H, Zhu C, et al. Cisplatin and doxorubicin dual-loaded mesoporous silica nanoparticles for controlled drug delivery. *RSC Adv*. 2016;6(96):94160–94169. doi:10.1039/C6RA17213J

28. Arean CO, Vesga MJ, Parra JB, Delgado MR. Effect of amine and carboxyl functionalization of sub-micrometric MCM-41 spheres on controlled release of cisplatin. *Ceram I*. 2013;39(7):7407–7414.

29. Rimoldi I, Facchetti G, Lucchini G, Castiglioni E, Marchianò S, Ferri N. In vitro anticancer activity evaluation of new cationic platinum(II) complexes based on imidazole moiety. *Biorg Med Chem*. 2017;25(6):1907–1913. doi:10.1016/j.bmc.2017.02.010

30. Ferri N, Facchetti G, Pellegrino S, et al. Promising antiproliferative platinum(II) complexes based on imidazole moiety: synthesis, evaluation in HCT-116 cancer cell line and interaction with Ctr-1 Met-rich domain. *Biorg Med Chem*. 2015;23(10):2538–2547. doi:10.1016/j.bmc.2015.03.044

31. Kang T, Park Y, Choi K, Lee JS, Yi J. Ordered mesoporous silica (SBA-15) derivatized with imidazole-containing functionalities as a selective adsorbent of precious metal ions. *J Mater Chem*. 2004;14(6):1043–1049. doi:10.1039/b315829b

32. Abolmaali SS, Tamaddon AM, Dinarvand R. Nano-hydrogels of methoxy polyethylene glycol-grafted branched polyethylenimine via biodegradable cross-linking of Zn2+-ionomer micelle template. *J Nanopart Res*. 2013;15(12):2134. doi:10.1007/s11051-013-2134-z

33. Abolmaali SS, Tamaddon A, Najafi H, Dinarvand R. Effect of l-Histidine substitution on Sol–Gel of transition metal coordinated poly ethylenimine: synthesis and biochemical characterization. *J Inorg Organomet Polym Mater*. 2014;24(6):977–987. doi:10.1007/s10904-014-0067-3

34. Abolmaali SS, Tamaddon AM, Mohammadi S, Amoozgar Z, Dinarvand R. Chemically crosslinked nanogels of PEGylated poly ethyleneimine (l-histidine substituted) synthesized via metal ion coordinated self-assembly for delivery of methotrexate: cytocompatibility, cellular delivery and antitumor activity in resistant cells. *Mater Sci Eng C*. 2016;62:897–907. doi:10.1016/j.msec.2016.02.045

35. Cheraghipour E, Tamaddon AM, Javadpour S, Bruce IJ. PEG conjugated citrate-capped magnetite nanoparticles for biomedical applications. *J Magn Magn Mater*. 2013;328:91–95. doi:10.1016/j.jmmm.2012.09.042

36. Mahmoodi M, Behzad-Behbahani A, Sharifzadeh S, Abolmaali SS, Tamaddon A. Co-condensation synthesis of well-defined mesoporous silica nanoparticles: effect of surface chemical modification on plasmid DNA condensation and transfection. *IET Nanobiotechnol.* 2017;11(8):995–1004. doi:10.1049/iet-nbt.2017.0078

37. Lee JS, Yim J-H, Jeon J-K, Ko YS. Polymerization of olefins with single-site catalyst anchored on amine-functionalized surface of SBA-15. *Catal Today.* 2012;185(1):175–182. doi:10.1016/j.cattod.2011.12.003

38. Li Q, Yue Q-Y, Su Y, Gao B-Y, Sun H-J. Equilibrium, thermodynamics and process design to minimize adsorbent amount for the adsorption of acid dyes onto cationic polymer-loaded bentonite. *Chem Eng J.* 2010;158(3):489–497. doi:10.1016/j.cej.2010.01.033

39. Allen SJ, McKay G, Porter JF. Adsorption isotherm models for basic dye adsorption by peat in single and binary component systems. *J Colloid Interface Sci.* 2004;280(2):322–333. doi:10.1016/j.jcis.2004.08.078

40. Jaroniec M. Adsorption on heterogeneous surfaces: the exponential equation for the overall adsorption isotherm. *Surf Sci.* 1975;50(2):553–564. doi:10.1016/0039-6028(75)90044-8

41. Vijayaraghavan K, Padmesh TVN, Palanivelu K, Velan M. Biosorption of nickel(II) ions onto Sargassum wightii: application of two-parameter and three-parameter isotherm models. *J Hazard Mater.* 2006;133(1):304–308. doi:10.1016/j.jhazmat.2005.10.016

42. Abolmaali S, Tamaddon A, Kamali-Sarvestani E, Ashraf M, Dinarvand R. Stealth nanogels of histinylated poly ethyleneimine for sustained Delivery of methotrexate in collagen-induced arthritis model. *Pharm Res.* 2015;32(10):3309–3323. doi:10.1007/s11095-015-1708-0

43. Farkhani SM, Shirani A, Mohammadi S, Zakeri-Milani P, Mojarrad JS, Valizadeh H. Effect of poly-glutamate on uptake efficiency and cytotoxicity of cell penetrating peptides. *IET Nanobiotechnol.* 2016;10(2):87–95. doi:10.1049/iet-nbt.2015.0030

44. Zarrin A, Sadighian S, Rostamizadeh K, et al. Design, preparation, and in vitro characterization of a trimodally-targeted nanomagnetic onco-theranostic system for cancer diagnosis and therapy. *Int J Pharm.* 2016;500(1):62–76. doi:10.1016/j.ijpharm.2015.12.051

45. Silva VAJ, Andrade PL, Silva MPC, D A B, Valladares LDLS, Aguiar JA. Synthesis and characterization of Fe3O4 nanoparticles coated with fucan polysaccharides. *J Magn Magn Mater.* 2013;343:138–143. doi:10.1016/j.jmmm.2013.04.062

46. Otokesh S, Kolvari E, Amoozadeh A, Koukabi N. Magnetic nanoparticle-supported imidazole tribromide: a green, mild, recyclable and metal-free catalyst for the oxidation of sulfides to sulfoxides in the presence of aqueous hydrogen peroxide. *RSC Adv.* 2015;5(66):53749–53756. doi:10.1039/C5RA07530K

47. Tao C, Zhu Y. Magnetic mesoporous silica nanoparticles for potential delivery of chemotherapeutic drugs and hyperthermia. *Dalton Trans.* 2014;43(41):15482–15490. doi:10.1039/C4DT01984A

48. Martinez DST, Paula AJ, Fonseca LC, et al. Monitoring the hemolytic effect of mesoporous silica nanoparticles after human blood protein corona formation. *Eur J Inorg Chem.* 2015;2015(27):4595–4602. doi:10.1002/ejic.201500573

49. Moore TL, Rodriguez-Lorenzo L, Hirsch V, et al. Nanoparticle colloidal stability in cell culture media and impact on cellular interactions. *Chem Soc Rev.* 2015;44(17):6287–6305. doi:10.1039/C4CS00487F

50. Kaasalainen M, Aseyev V, von Haartman E, et al. Size, stability, and porosity of mesoporous nanoparticles characterized with light scattering. *Nanoscale Res Lett.* 2017;12(1):74. doi:10.1186/s11671-017-1853-y

51. Sun D, Kang S, Liu C, Lu Q, Cui L, Hu B. Effect of zeta potential and particle size on the stability of SiO2 nanospheres as carrier for ultrasound imaging contrast agents. *Int J Electrochem Sci.* 2016;11(10):8520–8529. doi:10.20964/2016.10.30

52. Paula AJ, Silveira CP, Martinez DST, et al. Topography-driven bionano-interactions on colloidal silica nanoparticles. *ACS Appl Mater Interfaces.* 2014;6(5):3437–3447. doi:10.1021/am405594q

53. Vivero-Escoto JL, Elnagheeb M. Mesoporous silica nanoparticles loaded with cisplatin and phthalocyanine for combination chemotherapy and photodynamic therapy in vitro. *Nanomaterials (Basel, Switzerland).* 2015;5(4):2302–2316. doi:10.3390/nano5042302

54. Gu J, Su S, Li Y, He Q, Zhong J, Shi J. Surface modification−complexation strategy for cisplatin loading in mesoporous nanoparticles. *J Phys Chem Lett.* 2010;1(24):3446–3450. doi:10.1021/jz101483u

55. Thepphankulngarm N, Wonganan P, Sapcharoenkun C, Tuntulani T, Leeladee P. Combining vitamin B12 and cisplatin-loaded porous silica nanoparticles via coordination: a facile approach to prepare a targeted drug delivery system. *New J Chem.* 2017;41(22):13823–13829. doi:10.1039/C7NJ02754K

56. Wan X, Zhang G, Liu S. pH-disintegrable polyelectrolyte multilayer-coated mesoporous silica nanoparticles exhibiting triggered co-release of cisplatin and model drug molecules. *Macromol Rapid Commun.* 2011;32(14):1082–1089. doi:10.1002/marc.201100198

57. Zhang W, Shen J, Su H, et al. Co-delivery of cisplatin prodrug and chlorin e6 by mesoporous silica nanoparticles for chemo-photodynamic combination therapy to combat drug resistance. *ACS Appl Mater Interfaces.* 2016;8(21):13332–13340. doi:10.1021/acsami.6b03881

58. Desta MB. Batch sorption experiments: Langmuir and Freundlich isotherm studies for the adsorption of textile metal ions onto teff straw (Eragrostis tef) agricultural waste. *J Thermodyn.* 2013;2013:6. doi:10.1155/2013/375830

59. Gu J, Liu J, Li Y, Zhao W, Shi J. One-pot synthesis of mesoporous silica nanocarriers with tunable particle sizes and pendent carboxylic groups for cisplatin delivery. *Langmuir.* 2013;29(1):403–410. doi:10.1021/la3036264

60. Ukmar T, Maver U, Planinšek O, Kaučič V, Gaberšček M, Godec A. Understanding controlled drug release from mesoporous silicates: theory and experiment. *J Control Release.* 2011;155(3):409–417. doi:10.1016/j.jconrel.2011.06.038

61. Wu IY, Bala S, Škalko-Basnet N, Di Cagno MP. Interpreting non-linear drug diffusion data: utilizing Korsmeyer-Peppas model to study drug release from liposomes. *Eur J Pharm Sci.* 2019;138:105026. doi:10.1016/j.ejps.2019.105026

62. Yildirim A, Ozgur E, Bayindir M. Impact of mesoporous silica nanoparticle surface functionality on hemolytic activity, thrombogenicity and non-specific protein adsorption. *J Mater Chem B.* 2013;1(14):1909–1920. doi:10.1039/c3tb20139b

63. Lin Y-S, Haynes CL. Impacts of mesoporous silica nanoparticle size, pore ordering, and pore integrity on hemolytic activity. *J Am Chem Soc.* 2010;132(13):4834–4842. doi:10.1021/ja910846q

64. Helleman J, Burger K, Hamelers IHL, et al. Impaired cisplatin influx in an A2780 mutant cell line: evidence for a putative, cis-configuration-specific, platinum influx transporter. *Cancer Biol Ther.* 2006;5(8):943–949. doi:10.4161/cbt.5.8.2876

65. Sun LM, Liu YC, Li W, et al. Nivolumab effectively inhibit platinum-resistant ovarian cancer cells via induction of cell apoptosis and inhibition of ADAM17 expression. *Eur Rev Med Pharmacol Sci.* 2017;21(6):1198–1205.

66. Pan B, Yao K-S, Monia BP, et al. Reversal of cisplatin resistance in human ovarian cancer cell lines by a c-jun antisense oligodeoxynucleotide (ISIS 10582): evidence for the role of transcription factor overexpression in determining resistant phenotype. *Biochem Pharmacol.* 2002;63(9):1699–1707. doi:10.1016/S0006-2952(02)00841-9

67. Nur S, Rahman SA, Abdul Wahab N, Malek A. In vitro morphological assessment of apoptosis induced by antiproliferative constituents from the rhizomes of Curcuma zedoaria. *Evid Based Complement Alternat Med.* 2013;2013:1–14.

68. Liu K, Liu P-C, Liu RZ, Wu X. Dual AO/EB staining to detect apoptosis in osteosarcoma cells compared with flow cytometry. *Med Sci Monit Basic Res*. 2015;21:15–20. doi:10.12659/MSMBR.893327

69. Thapa B, Diaz-Diestra D, Beltran-Huarac J, Weiner BR, Morell G. Enhanced MRI T2 relaxivity in contrast-probed anchor-free PEGylated iron oxide nanoparticles. *Nanoscale Res Lett*. 2017;12 (1):312. doi:10.1186/s11671-017-2084-y

70. Mishra SK, Kumar BSH, Khushu S, Tripathi RP, Gangenahalli G. Increased transverse relaxivity in ultrasmall superparamagnetic iron oxide nanoparticles used as MRI contrast agent for biomedical imaging. *Contrast Media Mol I*. 2016;11(5):350–361. doi:10.1002/cmmi.1698

71. Khalkhali M, Rostamizadeh K, Sadighian S, Khoeini F, Naghibi M, Hamidi M. The impact of polymer coatings on magnetite nanoparticles performance as MRI contrast agents: a comparative study. *Daru*. 2015;23(1):015–0124. doi:10.1186/s40199-015-0124-7

72. Thapa B, Diaz-Diestra D, Santiago-Medina C, et al. T1- and T2-weighted magnetic resonance dual contrast by single core truncated cubic iron oxide nanoparticles with abrupt cellular internalization and immune evasion. *ACS Appl Bio Mater*. 2018;1(1):79–89. doi:10.1021/acsabm.8b00016